Spiral patterns, spiral breakup, and zigzag spirals in an optical device

Martine Le Berre, Elisabeth Ressayre, and Andrée Tallet

Laboratoire de Photophysique du CNRS, Bâtiment. 210, Université de Paris-Sud, 91405-Orsay, Cedex, France

Mustapha Tlidi

Optique Nonlinéaire Théorique, Université Libre de Bruxelles, Campus de la Plaine, C.P. 231, 1050 Bruxelles, Belgium

Above the first lasing threshold the degenerate optical parametric oscillator with saturable absorber displays successive Hopf and Turing instabilities. Various spiral patterns and defect turbulent patterns are numerically observed on the light intensity profiles. Close to the Hopf threshold, a normal form is derived which leads to a complex Ginzburg-Landau equation where a bi-Laplacian instead of a Laplacian drives the formation of spirals. At resonance the predictions of the normal form are compared with the numerical observations of the full equations. Above the Hopf threshold, the spirals destabilize, breaking into slowly evolving patterns with small spirals and filaments. Further above the threshold, when both the Turing and Hopf bifurcations interplay, a new spiral pattern emerges, with large notched arms.

I. INTRODUCTION

A large variety of spiral patterns observed in nature (shells, sunflowers, galaxies, etc.) and in the laboratory have motivated extensive work to understand what such diverse structures have in common. It was shown that the dynamical processes leading to the formation of spirals can be quite different and depend on the specific features of systems [1], even if the spirals are identical from the topological point of view. In optics a lot of effort was done to observe and to understand these fascinating patterns, theoretically and experimentally. There are two sorts of problems, one concerning the propagation of vortices in nonlinear media, which is ruled out by the nonlinear Schrödinger Eq. [2], and the other one, like here, concerns the formation of vortices in nonlinear resonators. Spiral waves were first predicted by Coullet *et al.* [3] who show that the Maxwell-Bloch equations for class-*A* lasers with large Fresnel number display numerical solutions with zero-intensity points—i.e., phase defects. The authors prove that the laser equations can be reduced to the famous complex Ginzburg-Landau (CGL) equation close to the onset of lasing and for negative detuning. This equation is known to be a paradigm for the study of spirals, vortices and defect turbulence solutions [4,5], in fluid mechanics. Such a link between lasers and fluids was extended to the case of small positive detuning where traveling waves are favored, leading to a complex Swift-Hohenberg (CSH) equation, which was recognized as the "universal description" of lasers dynamics [6]. The CSH equation was also derived for photorefractive oscillators [7], for a laser with injected signal [8], and for nondegenerate parametric oscillators [9].

The first experimental evidence of optical vortices was carried out in resonators with small Fresnel number [10]. These experiments were described with the help of transverse empty resonator modes which are linear modes. Later on, nonlinear defect patterns were observed in resonators with photorefractive medium first with plane mirrors [11], then using self-imaging resonators [7]. The latter experiment displays patterns in qualitative agreement with those of the CSH-laser equation. Close to the lasing threshold, a square lattice of vortices of alternating charge (like an alkali-halide crystal) is observed. As the pump intensity increases, the appearance of mobile defects leads to an irregular lattice, and finally domains of traveling waves separated by a row of vortices are formed far away from threshold. Other spiral waves formation have been reported in a coherently pumped three-level laser [12].

All the above mentioned optical spirals can be visualized only in the real (or the imaginary) part or in the phase of the field. They are called phase spirals. However, spiral structures and spiraling fronts can exist in the intensity field profile. Indeed, spiral intensity structures were first reported in nonlinear optics by Lodahl, Bache, and Saffman [13], in the internally pumped optical parametric oscillator (IPOPO). The linear stability analysis shows that these spirals arise as a result of the existence of a secondary Hopf bifurcation with a finite wave number and appear well above the threshold. A striking counterclockwise rotating spiral intensity pattern was recently observed experimentally in a semicavity with sodium vapor in presence of inhomogeneous pumping and boundary effects [14]. The numerical solutions, which agree with the experiment, allow to interpret the multiarmed spiraling patterns as a result of the interaction between Hopf and Turing instabilities.

Other classes of spirals appearing in the intensity of the field are the spiraling fronts [1], like those found in the Faraday experiment or in periodically forced chemical systems [15]. This behavior has been reported numerically in the type-II OPO with four interacting fields [16] and also in the optical parametric oscillator that converts a pump field at frequency 3ω into signal and idler fields at frequency 2ω and ω (3:2:1 OPO) with the help of a second crystal generating a second harmonic [17]. The three-armed spirals numerically observed in the latter case were explained by reducing the model equations to a CGL equation with forcing. The spiraling fronts spontaneously nucleate from noise at points where domain walls connecting the different phase states coalesce [18].

We consider the degenerate optical parametric oscillator (DOPO) under the presence of the saturable absorber (SA). Due to the richness of its dynamical behavior, this system has been a subject of recent investigations. Stationary and/or time-dependent localized structures and mixed-mode solutions [19], moving asymmetric solitons [20,21], and the stabilization of the phase locked hexagonal structures below the lasing threshold [21,22] are the phenomena that were predicted.

In this paper, we show numerically that this system supports spiral structures and defect turbulent patterns in the intensity profiles of both signal and pump fields. As in the case of the IPOPO [13], the intensity spirals are formed above a secondary Hopf bifurcation. However, the linear analysis proves that they are found in a different dynamical regime; namely, they exist just above the Hopf instability threshold associated with a zero wave number and not with a finite wave number. A weakly nonlinear analysis is performed in the simple situation where both fields are resonant with the optical cavity—i.e., zero cavity detunings. In that regime, analytical calculations in the vicinity of the critical point associated with the Hopf bifurcation allow us to construct a normal-form equation: namely, a CGL-type equation where the spatial coupling is provided by the bi-Laplacian, the Laplacian term being absent. We extend this study to near-resonant conditions, which leads to add to the normal form a Laplace operator with a small coefficient proportional to the detuning parameter. This contribution has only a minor effect on the intensity spiral formation. For several sets of parameters, the predictions of the nonlinear analysis are compared with the numerical simulation of the mean field model presented in this paper. In addition we performed a comparison with the full propagation model [see Eqs. (1)—(6) of [21]]. The agreement is good close to the Hopf threshold. Far from that threshold the nonlinear analysis is no longer valid. In that regime, the spiral structures break up into spiraling wormlike filament. This behavior is attributed to the growth of new spatial modes when the homogeneous steady state becomes unstable with respect to the Turing instability. More importantly, in the regime of strong interaction between Hopf and Turing modes, spiral intensity structures developed notched arms, named zigzag spirals.

In the next section, we briefly introduce the model equations for the degenerate optical parametric oscillator (DOPOSA) together with the linear and weakly nonlinear analysis leading to the complex order parameter amplitude equation. The numerical results and comparison with the analytical predictions are presented in Sec. III. Finally, we conclude in Sec IV.

II. LINEAR AND WEAKLY NONLINEAR ANALYSIS

A. Model equations

We suppose that the frequency conversion process takes place in a ring cavity with flat mirrors that is resonant at both frequencies (parametric amplification). An external field E at frequency ω_0 is injected into the cavity where it undergoes the down-conversion process: one photon with frequency ω_0 is absorbed and two photons with frequency $\omega_0/2$ are emit-

ted. We assume the presence of a saturable absorber modeled by a collection of two-level atoms that leads to an intensity-dependent effective absorption coefficient, supposed to act selectively on the frequency $\omega_0/2$. We assume that the medium relaxes much faster than the cavity field. We limit our study to the type-I parametric amplification that does not involve polarization degrees of freedom due to the birefringence of the $\chi^{(2)}$ crystal. In the good cavity limit and under the mean-field approximation, the combined influence of the parametric amplification and the saturable absorber is described by the following set of dimensionless partial differential equations [21]

$$\partial_t A_0 = -\gamma[(1 + i\Delta_0)A_0 + A_1^2 - E] + \frac{i}{2}\Delta_T A_0, \quad (1)$$

$$\partial_t A_1 = -(1 + i\Delta_1)A_1 + A_1^* A_0 - \frac{RA_1}{1 + S|A_1|^2} + i\Delta_T A_1. \quad (2)$$

The complex amplitudes $A_{0,1}$ are the normalized slowly varying envelopes of the pump and signal fields at frequency ω_0, and $\omega_0/2$, respectively. The parameters $\Delta_{0,1}$ are the cavity detunings of the fields. R is the field-matter interaction coefficient in the absorber, and S measures its saturability. γ is the ratio of transmitivity for the two fields, and Δ_T is the Laplacian acting on the transverse coordinates $\mathbf{r} = (x, y)$.

For simplicity, we will assume that both frequencies ω_0 and $\omega_0/2$ are perfectly resonant with the cavity $\Delta_0 = \Delta_1 = 0$. As we shall see in the following, our analysis will be valid also for small detuning cases. At resonance, when the control parameter E increases, the first bifurcation occurs at the lasing threshold $E_{th} = 1 + R$. Above that critical point, two equivalent homogeneous steady-state solutions (HSS's) exist, $\bar{A}_0, \pm\bar{A}_1$. For real values of E, the solutions are real and satisfy the relations $\bar{A}_0 = E - \bar{I}_1$ and $E = 1 + \bar{I}_1 + R/(1 + S\bar{I}_1)$, $\bar{I}_1 = |\bar{A}_1|^2$. The linear stability analysis of the HSS's shows the existence of a soft and a hard type of modes that can affect the stability of these HSS's. The former refers to mode arising from a modulational (often called a Turing) instability leading to steady-state periodic dissipative structures, while the latter refers to oscillatory instability such as a Hopf bifurcation associated with the homogeneous self-pulsing. The critical wave number at the Turing instability and the frequency of the homogeneous Hopf bifurcation as well as the thresholds associated with these instabilities are given in [21]. The relative separation between these two thresholds, on the steady-state response curve, is determined by the parameter values R and S. The interaction between these instabilities has been studied by using the normal-form analysis in the regime where they are close one to another [19]. Here we consider situations where the Hopf bifurcation occurs before the Turing one, as the control parameter E is increased. The results from the linear stability analysis of the HSS are illustrated in Fig. 1 where the growth rate is plotted as a function of the wave number. This curve is obtained for the input field in the parameter range $E_H < E < E_T$ where E_H and E_T are the thresholds associated with Hopf and Turing instabilities, respectively. The left curve domain, associated with the Hopf
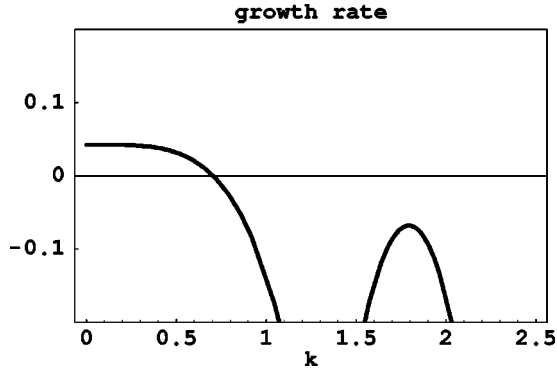
FIG. 1. Linear stability analysis of the lasing solution of Eqs. (1) and (2): maximum growth rate versus the wave number. Parameters are $R=4.5$, $S=0.1$, $\gamma=1$, and $E=6.5$. The left domain corresponds to the Hopf bifurcation with a frequency of order unity, and the right domain corresponds to a Turing instability with zero frequency.

instability, has a most unstable mode with zero wave number ($k=0$) and a finite frequency ($\omega=\omega_H$), whereas the right one, associated with the Turing instability, has a finite wave number ($k_T \neq 0$) and a zero frequency ($\omega=0$). In the following subsection, we suppose that Hopf and Turing thresholds are well separated from one to another, and we construct a normal form valid in the vicinity of the homogeneous Hopf bifurcation characterized by $k=0$, $\omega=\omega_H$.

B. Weakly nonlinear analysis

We focus on the case of zero detunings and generalize the calculations hereafter to finite but small detunings. For this purpose, we introduce deviations from the HSS as $A_{0,1}=\bar{A}_{0,1}+a_{0,1}$. Inserting these relations in Eqs. (1) and (2), we obtain

$$\partial_t a_0 = -\gamma a_0 - \gamma(2\bar{A}_1 a_1 + a_1^2) + \frac{i}{2}\Delta_T a_0, \quad (3)$$

$$\partial_t a_1 = -a_1 + (\bar{A}_0 a_1^* + \bar{A}_1^* a_0) + a_0 a_1^* - RF(a_1, a_1^*) + i\Delta_T a_1, \quad (4)$$

$$F(a_1, a_1^*) = \frac{\bar{A}_1 + a_1}{1 + S|\bar{A}_1 + a_1|^2} - \frac{\bar{A}_1}{1 + S|\bar{A}_1|^2}. \quad (5)$$

We then decompose $a_{0,1}$ into its real and imaginary parts as $a_{0,1}=x_{0,1}+iy_{0,1}$. Equations (3) and (4) lead to the set of equations of the form $\partial_t u = f(u, \Delta_T, E)$ with $u=(x_0, x_1, y_0, y_1)^{tr}$, where the superscript tr means transpose vector and $f=f_u u + N(u, \Delta_T)$. The linear part f_u is composed of two diagonal 2×2 blocks,

$$f_u = \begin{pmatrix} -\gamma & -2\gamma\bar{A}_1 & 0 & 0 \\ \bar{A}_1 & \zeta & 0 & 0 \\ 0 & 0 & -\gamma & -2\gamma\bar{A}_1 \\ 0 & 0 & \bar{A}_1 & \gamma' \end{pmatrix}, \quad (6)$$

with $\zeta=2RS\bar{I}_1/D^2$, $\gamma'=-2(1+R/D)$, and $D=1+S|\bar{A}_1|^2$.

The Hopf bifurcation occurs when one or more eigenvalue has a vanishing real part ($\lambda=i\omega_H$). The determination of the Hopf threshold involves the 2×2 matrix located in the left upper quadrant only. The eigenvalue problem $\partial_t u = \lambda u$ gives rise to the relation $\gamma=\zeta$ which determines the Hopf threshold intensity

$$\bar{A}_{1H}^2 = \frac{1}{S}\left[\frac{R}{\gamma} - 1 \pm \sqrt{\frac{R}{\gamma}\left(\frac{R}{\gamma} - 2\right)}\right] \quad (7)$$

and the corresponding critical frequency $\omega_H^2=(2\bar{A}_{1H}^2-\gamma)\gamma$. At that Hopf bifurcation the eigenvector is $(p_0, p_1, 0, 0)^{tr}e^{i\omega_H t}$.

To construct the amplitude equation, we consider the following expansions in terms of a small parameter ε measuring the distance from the Hopf bifurcation: $E=E_H+\varepsilon^2$ and $u=\varepsilon u^{(1)}+\varepsilon^2 u^{(2)}+\varepsilon^3 u^{(3)}+\cdots$, with $E_H=1+\bar{I}_{1H}+R/(1+S\bar{I}_{1H})$ and $u^{(1)}=A(p_0, p_1, 0, 0)^{tr}e^{i\omega_H t}$. We rescale time and space as $\partial_t=\partial_{t_0}+\varepsilon^2\partial_{t_2}+\cdots$ and $\partial_{x,y}=\varepsilon^{1/2}\partial_{X,Y}+\cdots$.

Proceeding on to the higher-order inhomogeneous problem, we derive the amplitude equation for the critical mode associated with the Hopf bifurcation by formulating the appropriate solvability conditions (see Appendix A)

$$\partial_t A = \varepsilon^2\mu A - c_3|A|^2 A - c_1\Delta_T^2 A, \quad (8)$$

with complex coefficients $\mu=\mu_r+i\mu_i$, $c_3=c_{3r}+ic_{3i}$, and $c_1=c_{1r}+ic_{1i}$. After rescaling, $\sqrt{c_{3r}/\epsilon^2\mu_r}Ae^{-i\mu_i t} \to A$, $\epsilon^2\mu_r t \to t$, $x^4\epsilon^2\mu_r/c_{1r} \to x^4$, and $y^4\epsilon^2\mu_r/c_{1r} \to y^4$, Eq. (8) becomes

$$\partial_t A = A - (1+ib)\Delta_T^2 A - (1+ic)|A|^2 A, \quad (9)$$

with $b=c_{1i}/c_{1r}$ and $c=c_{3i}/c_{3r}$. Equation (9) may be seen as a CGL type of equation with a bi-Laplacian or a CSH equation with a critical wave number equal to zero and no Laplacian term. The absence of a Laplacian in the amplitude equation (9) is due to the fact that Eqs. (1) and (2) are invariant by the transformation $x \to ix$, $A_0 \to A_0^*$, and $A_1 \to A_1^*$ at resonance. The parameters b and c are related to the physical parameters γ, R, S of Eqs. (1) and (2), but are independent of the input pump amplitude value. If, for example, we choose the parameters of Fig. 1—namely, $R=4.5$, $S=0.1$, and $\gamma=1$—the coefficients are $\mu=0.38+i0.82$, $c_3=0.94+i0.33$, and $c_1=0.17-i0.015$, leading to $b=-0.09$ and $c=0.35$.

In the case of small detunings $\Delta_{0,1}=\epsilon\Delta_{0,1}^{(1)}$, $\delta=\epsilon\delta^{(1)}$, one can easily show that Eq. (9) becomes, after rescaling, of the form

$$\partial_t A = A + d\Delta_T A - (1+ib)\Delta_T^2 A - (1+ic)|A|^2 A, \quad (10)$$

where the complex coefficient d is a linear combination of the detunings and the coefficients b and c are modified with respect to the expressions given above. The normal form (10) is an equation of the CSH type where the coefficient of the Laplacian term is small. In order to clarify the roles of the Laplacian and bi-Laplacian terms on the long-time dynamics of Eq. (9) we have compared the numerical solutions of Eqs. (9) and (10) and the CGL equation

$$\partial_t A = A + (1+ib)\Delta_T A - (1+ic)|A|^2 A. \quad (11)$$

To this end, we chose the parameters $b=4$ and $c=-1$, we use random initial conditions, and periodic boundaries in
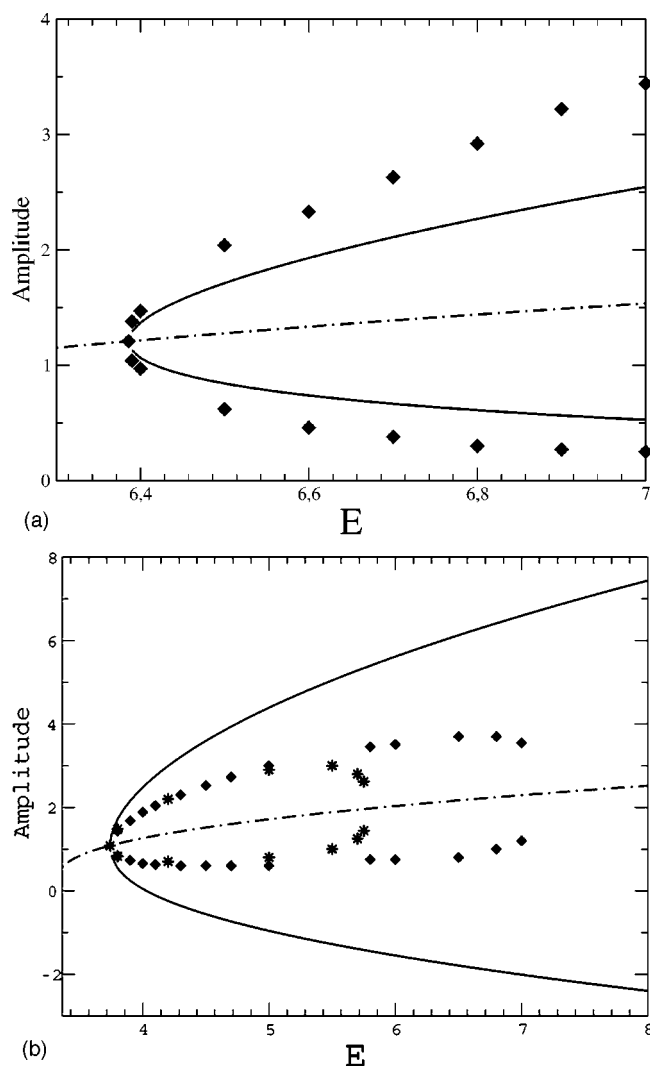
(a)

(b)

FIG. 2. Amplitude diagram of the limit cycle. Comparison between the numerical models and the nonlinear analysis prediction (solid line). Parameters are $R=4.5$, $S=0.1$, and $\gamma=1$ for (a) and $R=2.3$, $S=0.4$, and $\gamma=1$ for (b). The diamonds correspond to the limit cycle amplitude for the mean-field model, the stars for the propagation model. The dotted-dashed line in the middle draws the HSS amplitude.

both transverse directions. Under these conditions, Eq. (9) leads to a large stable spiral, while this case belongs to the defect turbulent regime of the CGL, Eq. (11), where no stable spiral exists. In the case of Eq. (10), with a small coefficient in front of the Laplacian operator, written as $d=\delta(1+ib)$, the final state is also a spiral for δ increasing up to 0.5. Therefore the Laplacian term in Eq. (10) plays a negligible role in the pattern selection mechanism, for small values of the detunings, that justifies to focus on the case of zero detunings.

Since Eq. (9) has not yet been investigated to our knowledge, we derive in Appendix B the condition for stability of plane-wave solutions of the form $A=Fe^{i(\mathbf{Q}\cdot\mathbf{r}-wt+\phi)}$, where the amplitude F and the frequency ω depend on the wave number $Q=|\mathbf{Q}|<1$, through the relations $F^2=1-Q^4$ and $\omega=c+(b-c)Q^4$. The homogeneous oscillating state $(Q=0)$, is
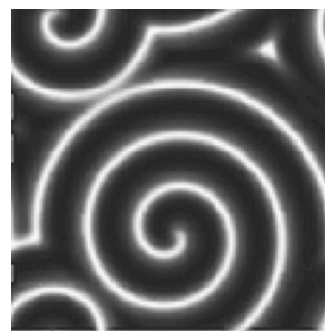

FIG. 3. Steadily rotating spiral for $R=4.5$, $S=0.1$, and $E=6.4$ obtained after a long transient, $dx=0.78$, and the grid is 128×128 points.

shown to be stable with respect to long-wavelength perturbations if

$$1+bc>0, \tag{12}$$

which is identical to the Benjamin-Feir relation for the usual CGL Eq. (11). As an example, the condition (12) is fulfilled for the parameter set chosen in Fig. 1 (cf. the b,c values given above), for which a flat intensity profile, oscillating homogeneously in time, is expected to be a solution of the DOPOSA equations.

III. NUMERICAL RESULTS

We performed numerical simulations of the mean-field model, Eqs. (1) and (2), and we extend our study to the propagation model that describes correctly the propagation of the fields through the two nonlinear media [see Eqs. (1)—(6) of [21]]. In this description, the fields are assumed to have equal group velocity inside both media. Our numerical analysis allows us not only to check the above theoretical predictions but also to check the validity of the mean-field approximation that is regularly used in nonlinear optics. Previous studies of localized pattern formation have revealed, however, that the mean-field approximation is valid for small intensity patterns only [21,23]. The mean-field model is solved by using a code based on a finite-difference implicit Crank-Nicholson scheme and the propagation model by using a split and step spectral method. In both models we use mostly periodic boundary conditions in the two-dimensional transverse plane, and the number of grid points is from 128×128 up to 512×512.

In the parameter range investigated here, four different solutions can be obtained for the same value of the pump amplitude $E>E_H$, depending on the initial conditions. Two of them are time-independent solutions, the localized structures and the periodic solutions. They result from a locking between the two equivalent out-of-phase signal solutions [24] and are not considered here. The two other solutions, which interest us, oscillate in time with frequency ω_H and are formed around one of the HSS's, the signal amplitude being positive (or negative) on the whole transverse plane. One of these solutions has a homogeneous profile; the other presents defects. The homogeneous oscillating solution, which is ex-
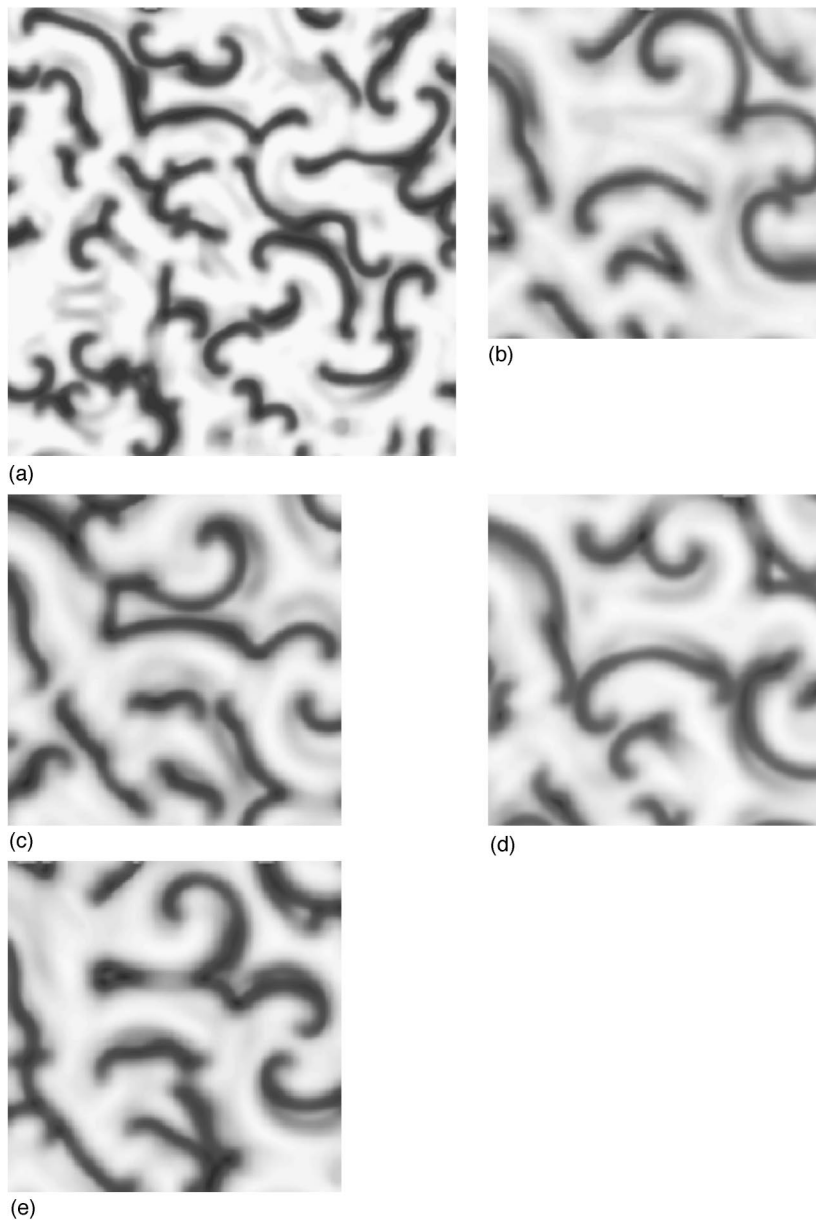
FIG. 4. Spiral break up regime. Evolution during one period. (a) t, (b) $t+T/5$, (c) $t+2T/5$, (d) $t+3T/5$, and (e) $t+4T/5$. (b)—(e) show one-fourth part of the full pattern [upper part in the middle of (a)]. Parameters are the same as in Fig. 3, except $E=7.1$, $dx=0.5$, and the grid is 200×200 points.

pected to be stable if the condition $1+bc>0$ is fulfilled (cf. Sec. II), displays in-phase oscillating time traces in the whole transverse plane. In the case of solutions with defects, local time traces are phase shifted. We shall focus now on these two time-dependent solutions.

In order to obtain a positive value for $\mathrm{Re}(A_1)$ and avoid the formation of the solutions connecting the two HSS branches, we start from the initial condition $A_0(t=0,x,y)=\bar{A}_0$, $A_1(t=0,x,y)=\bar{A}_1+\chi(x,y)$, where the noise $\chi(x,y)$ is not too large (its standard deviation σ_χ is always smaller than $\bar{A}_1$). Below the Hopf threshold, $E<E_H$, the initial noise decays, and the final solution is $(\bar{A}_0,\bar{A}_1)$, indicating that the Hopf bifurcation occurs supercritically. Above the Hopf threshold, $E>E_H$, the final solution depends on σ_χ.

In the two next subsections, we describe the numerical solutions of the DOPOSA equations [Eqs. (1) and (2) and the propagation model] for different values of parameters R and

S, the ratio of transmitivity for the two fields γ being fixed to $\gamma=1$.

A. Study of the homogeneous solution

For small noise, $\sigma_\chi \ll \bar{A}_1$ and for $E>E_H$, numerical solutions of the DOPOSA equations show the same behavior for the values of parameters that we have chosen: long-wavelength modulations appear in the transient, whose amplitude tends to zero asymptotically as time increases. This behavior is in agreement with our nonlinear analysis. Indeed when using the values of coefficients b and c derived in Sec. II B, we check that the relation $1+bc>0$ is fulfilled, indicating that our numerical investigation concerns the stable Benjamin-Feir domain. The bifurcation diagrams given in Figs. 2(a) and 2(b), for two different cases, shows that the numerical amplitude of the limit cycle agrees with the prediction of the nonlinear analysis $|A(E)|=\sqrt{(E-E_H)\mu_r/c_{3r}}$
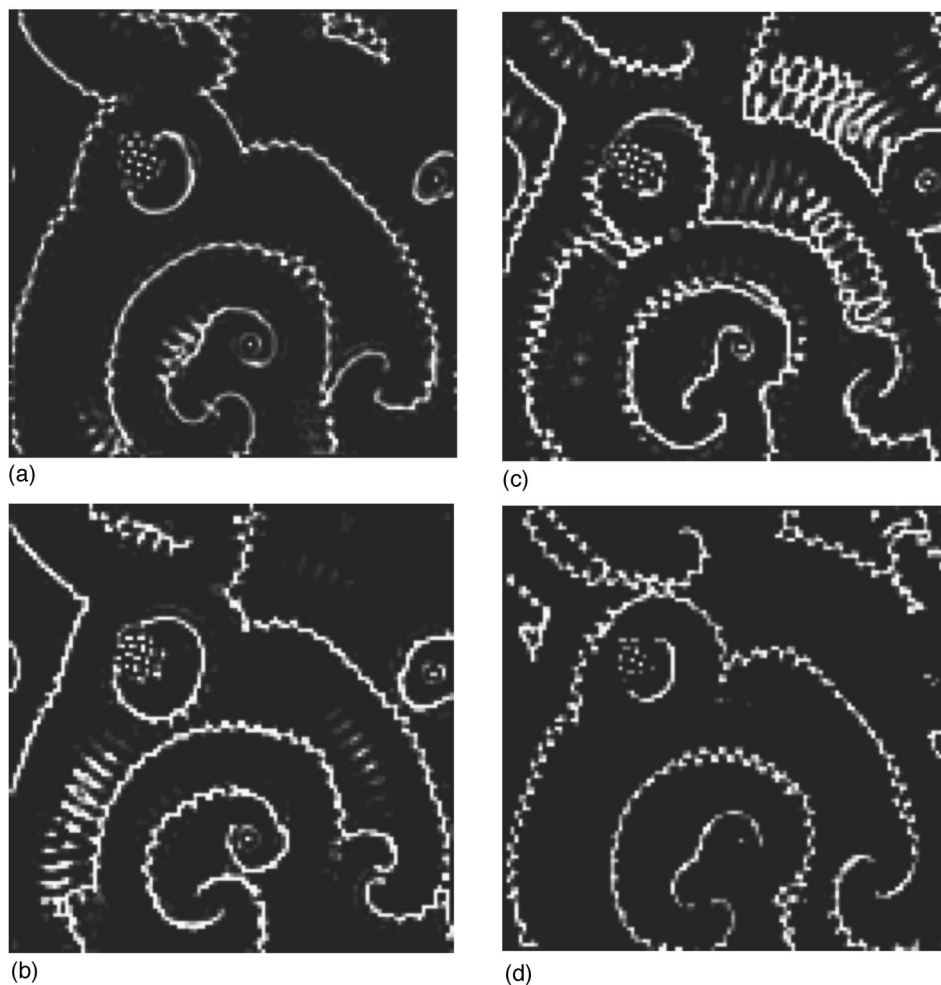
FIG. 5. Zigzag spirals. Evolution of the signal intensity along one period. (a) t, (b) $t+T/4$, (c) $t+2T/4$, and (d) $t+3T/4$. Parameters are the same as in Fig. 3, except for $E=8.8$. Positive maxima are on the spiral arms; few negative peaks are visible. The grid is 512×512 and $dx=0.234$.

close to E_H. The curves obtained with the DOPOSA models depart from the theoretical predictions of the weakly nonlinear analysis for large $E-E_H$. Moreover, in this regime, the mean-field model clearly fails to describe large-amplitude solutions because propagation effects become significant, as expected from our previous studies of localized structures [2]. For example, Fig. 2(b) shows that the two models agree
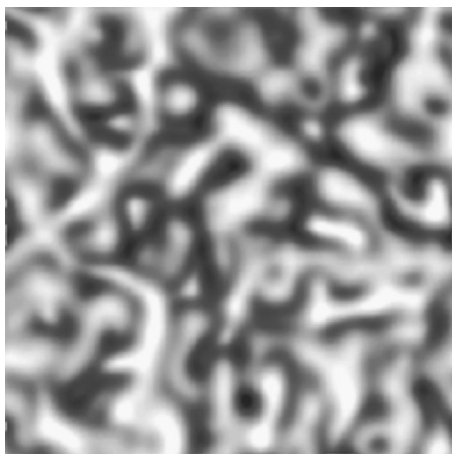

FIG. 6. Chaos. Parameters are $R=2.3$, $S=0.4$, and $E=5.5$ ($E_H=3.74$). The grid is 256×256 with $dx=0.50$.

for $E\lesssim5.5$ only. The prediction of the weakly nonlinear analysis presented in Sec. II B. shows that the frequency of the limit cycle, i.e., spatially homogeneous solutions oscillating in time, depends on the control parameter values according to $\omega(E)=\omega_H+\mu_i(E-E_H)$. Our numerical simulations are in good agreement with this prediction. For example in the case Fig. 2(a), the deviation between the numerics and the theory is about 10% at $E=8.8$, which is noticeably smaller than the deviation of the amplitude.

B. Solutions with defects

For moderate noise, $\sigma_\chi\lesssim\bar{A}_1$, numerical simulations of the DOPOSA equations show that spiral patterns are formed close to the Hopf threshold ($E\gtrsim E_H$), as illustrated in Fig. 3, for the parameter values of Fig. 2(a), $R=4.5$ and $S=0.1$. During one period the spirals rotate with the frequency ω_H around their core. The spiral core amplitude is constant and equal to the HSS value. We have checked that periodic snapshots correspond to the quasifrozen spiral solutions of Eq. (9) for the corresponding b and c values given in Sec. II. These spirals also occur in the numerical simulations of the CGL, Eq. (11), for small values of b and c and were recently identified as a liquid vortex state [26]. For the values chosen here for R and S, the Hopf and Turing instabilities have

threshold values $E_H=6.385$ and $E_T \simeq 7.1$, respectively. Increasing the control parameter E, the time trace becomes more and more chaotic and the quasifrozen spirals progressively break into smaller ones. When approaching the Turing threshold—i.e., $E \lesssim E_T$—only wormlike and spiraling filaments exist. This behavior is illustrated in Fig. 4. During one period, the collision and separation processes of neighboring filaments is represented in Fig. 4 at successive times $t + nT/5$, $n=0, 1, 2, 3, 4$. The far-field pattern displays mainly components with wave numbers belonging to the whole Hopf domain (left domain of the linear analysis curve in Fig. 1). This spiral breakup pattern looks like those obtained close to the defect turbulent regime of CGL [4] or in chemistry [15,27]. Nevertheless, its slow dynamics differs from the CGL turbulent pattern one. Our results are closer to those previously reported in the physiological model describing the cardiac tissue [28], where the breakup of an isolated spiral led to a quasifrozen state of small spirals. But in this model, the breakup of the spiral was attributed to the large variations of the rotation period which do not occur in the DOPOSA.

For larger input field amplitude—i.e., for $E>E_T$—the arms become larger and get modulations. For $E \sim 8.5$, each arm splits into a central part and lateral damped wings. For $E \sim 8.7$, a new spiral pattern emerges with notched arms, somehow remiscent of the "zigzag spirals" found in a gas discharge device [29]. Its behavior is illustrated in Fig. 5, which clearly shows the behavior of the zigzag spirals during one period, with collision and separation processes. These high-intensity zigzag spirals coexist with few localized structures, which act as sources nucleating defects at time intervals equal to one period. Note that in Fig. 5, the real part of the signal field is positive everywhere, except around the extrema of the peaks where it is negative. The spatial Fourier spectrum displays a central spot, with wave numbers smaller than unity—i.e., belonging to the Hopf instability domain (left curve in Fig. 1)—and an outer ring which becomes more and more intense as E increases. In the ring the wave number values are comparable with those of the periodic stationary pattern solutions such as rolls, hexagons, or squares. Therefore the zigzag spirals are an example of mixed-mode solutions resulting from the interaction between the Hopf and Turing instabilities.

This result is confirmed by looking at the sequences obtained for other parameter values. Let us consider the case $R=4.5$ and $S=0.05$, where the Hopf and Turing thresholds are more separated than above. The spirals are not so beautiful as in the case of Figs. 3–5, but the same sequence of spirals, spiral portions, and zigzag spirals has been observed. Another case, $R=2.3$, $S=0.4$, corresponding to Fig. 2(b), is especially interesting because there is no Turing instability (for $E>E_H$ the growth rate of the Turing modes decreases with E, differently from the cases described above). Spirals are observed close to the Hopf threshold, but for $E \gg E_H$ no zigzag spirals appear, but chaotic structures with interlaced filaments and craters, as shown in Fig. 6.

In the numerical simulations, we checked that the mean-field model displays the same sequences as the propagation model. However, there are noticeable differences concerning the amplitude of the pattern and the range of its existence, as expected from our study in Fig. 2. Note that we have re-
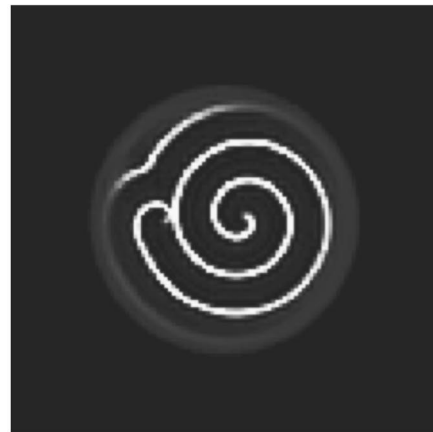
(a)
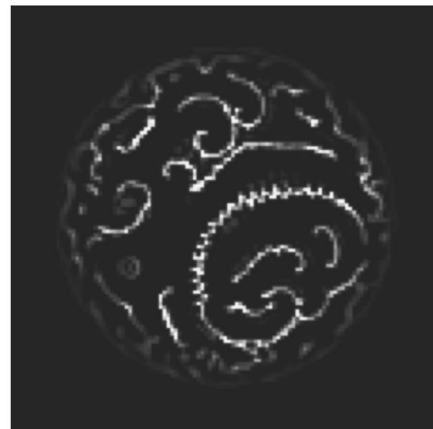
(b)

FIG. 7. Spirals with circular input beam. Intensity of the signal field, obtained with the propagation model. Parameters are $R=4.5$, $S=0.1$, and $\gamma=1$. (a) $E=6.4$, and grid is 256×256 points, $dx=0.58$. (b) $E=8.7$, and grid is 512×512 points, $dx=0.31$.

stricted our study to an isotropic system where the external field is a plane-wave beam. However, the inhomogeneities induced by the pump profile and the finite geometry are both important problems in optics. We show numerically that the formation of spiral patterns reported can also be obtained with a Gaussian or hyper-Gaussian profile of the input field amplitude. This numerical result is illustrated in Fig. 7. This problem has been discussed in the frame work of the CGL equation [30].

IV. CONCLUSION

We have investigated analytically and numerically the formation of spiral pattern in the degenerate optical parametric oscillator with a saturable absorber, which displays successive homogeneous Hopf (with a zero wave number) and Turing instabilities, with well-separated thresholds. We have performed a weakly nonlinear analysis in the vicinity of the Hopf bifurcation at the perfect resonance conditions—i.e., for zero cavity detunings. This procedure allows us to derive an amplitude equation of the Ginzburg-Landau type but with a bi-Laplacian rather than a simple Laplace operator. This derivation has been extended to more general

situations: namely, close to the resonant condition which is obtained for small detuning parameters. Close to the Hopf threshold the predictions of the normal form equation for the amplitude of the limit cycle and its frequency are in good agreement with the numerical solutions of the DOPOSA equations. Our analysis reveals that the stability criterion for the homogeneous oscillating solution is $1+bc>0$, like in the case of the CGL equation.

Numerical simulations show various patterns with defects, in particular stationary spirals close to the Hopf threshold E_H, evolving into small spiral portions as E approaches the Turing threshold E_T, then into a zigzag spiral pattern which is an example of a two-dimensional Hopf-Turing mixed-mode solutions.

The present study has emphasized the rich behavior of the DOPOSA in the regime of strong interaction between the Turing and the Hopf bifurcations. We have elucidated the formation of spirals close to E_H, but many interesting questions remain unsolved, such as properties of the disordered states and the transition leading to their formation [26,31].

APPENDIX A: AMPLITUDE EQUATION CLOSE TO E_H

Close to the Hopf threshold, we use the expansions given in Sec. II B just before Eq. (8) and the HSS expansion $(\bar{A}_0,\bar{A}_1,\bar{I}_1)=(\bar{A}_{0H},\bar{A}_{1H},\bar{I}_{1H})+\varepsilon^2(A_0^{(2)},A_0^{(2)},I_1^{(2)})$ with $\bar{A}_1^2=\bar{I}_1$. The eigenvector of the adjoint problem, associated with the submatrix

$$\begin{pmatrix} \gamma & -\bar{A}_{1H} \\ 2\gamma\bar{A}_{1H} & -\gamma \end{pmatrix}, \tag{A1}$$

with eigenvalue $i\omega_H$, is $(q_0,q_1,0,0)^{tr}e^{i\omega_H t}$. In the following we choose $p_0=(i\omega_H-\gamma)/\bar{A}_{1H}$, $q_0=p_1=1$, and $q_1=(i\omega_H+\gamma)/\bar{A}_{1H}$, which gives $p_0q_0+p_1q_1=2i\omega_H/\bar{A}_{1H}$.

The second-order expansion of the stationary solution provides $I_1^{(2)}=D^2/(D^2-RS)$, $A_0^{(2)}=-RSI_1^{(2)}/D^2$, $I_1^{(2)}/D^2$, and $A_1^{(2)},=I_1^{(2)}/2\bar{A}_1$, where the index $D=D_H$ (in the following, the index H is omitted when referring to the threshold value).

At order ε^2 the mean-field model writes $(\partial_{t_0}-f_u)u^{(2)}=g^{(2)}$ with

$$g^{(2)}=\begin{pmatrix} -\gamma(x_1^{(1)})^2 \\ x_0^{(1)}x_1^{(1)}-RF_x^{(2)} \\ \dfrac{1}{2}\Delta_T^{(1)}x_0^{(1)} \\ \Delta_T^{(1)}x_1^{(1)} \end{pmatrix}, \tag{A2}$$

where $F_x^{(2)}=t_f x_1^{(1)2}$, $t_f=4\bar{A}_1^3 S^2/D^3-3\bar{A}_1 S/D^2$, and the transverse Laplacian operator is such that $\Delta_{\perp(x,y)}=\varepsilon\Delta_{\perp(X,Y)}^{(1)}$. Equation (A2) gives

$$(\partial_{t_0}-f_u)u^{(2)}=A^2e^{2i\omega t}\begin{pmatrix} -\gamma p_1^2 \\ p_0p_1-Rt_f p_1^2 \\ 0 \\ 0 \end{pmatrix}+|A^2|$$

$$\times\begin{pmatrix} -2\gamma|p_1|^2 \\ p_0p_1^*+\text{c.c.}-2Rt_f|p_1|^2 \\ 0 \\ 0 \end{pmatrix}$$

$$+\Delta_T Ae^{i\omega t}\begin{pmatrix} 0 \\ 0 \\ p_0/2 \\ p_1 \end{pmatrix}+\text{c.c.} \tag{A3}$$

The solvability condition is fulfilled since $\partial_{t_1}u=\partial f/\partial E=0$.

The inverse matrix is

$$M_n=(ni\omega-f_u)^{-1}=\begin{pmatrix} a_-(n) & b(n) & 0 & 0 \\ c(n) & a_+(n) & 0 & 0 \\ 0 & 0 & a'_-(n) & b'(n) \\ 0 & 0 & c'(n) & a'_+(n) \end{pmatrix}, \tag{A4}$$

where $a_\pm(n)=(ni\omega\pm\gamma)/m_n$, $b(n)=-2\bar{A}_1\gamma/m_n$, $c(n)=\bar{A}_1/m_n$, $m_n=(ni\omega+\gamma)(ni\omega-\gamma)+2\gamma I_1$, $a'_\pm(n)=(ni\omega\pm\gamma')/m'_n$, $b'(n)=-2\bar{A}_1\gamma'/m'_n$, $c'(n)=\bar{A}_1/m'_n$, and $m'_n=(ni\omega+\gamma)(ni\omega-\gamma')+2\gamma I_1$.

A particular solution of Eq. (A3) is

$$u^{(2)}=A^2e^{2i\omega t}\begin{pmatrix} x_0^{(2,2\omega)} \\ x_1^{(2,2\omega)} \\ 0 \\ 0 \end{pmatrix}+|A|^2\begin{pmatrix} x_0^{(2,0)} \\ x_1^{(2,0)} \\ 0 \\ 0 \end{pmatrix}$$

$$+\Delta_T^{(2)}Ae^{i\omega t}\begin{pmatrix} 0 \\ 0 \\ y_0^{(2,\omega)} \\ y_1^{(2,\omega)} \end{pmatrix}+\text{c.c.}, \tag{A5}$$

with

$$x_0^{(2,2\omega)}=-\gamma p_1^2 a_-(2)+(p_0p_1-Rt_f p_1^2)b(2), \; x_1^{(2,2\omega)}$$

$$=-\gamma p_1^2 c(2)+(p_0p_1-Rt_f p_1^2)a_+(2),$$

$$x_0^{(2,0)} = -2\gamma|p_1^2|a_-(0) + (p_0 p_1^* + \text{c.c.} - 2Rt_f|p_1^2|)b(0),$$

$$x_1^{(2,0)} = -2\gamma|p_1^2|c(0) + (p_0 p_1^* + \text{c.c.} - 2Rt_f|p_1^2|)a_+(0),$$

$$y_0^{(2,\omega)} = \frac{1}{2}p_0 a_-'(1) + p_1 b'(1), \quad y_1^{(2,\omega)} = \frac{1}{2}p_0 c'(1) + p_1 a_+'(1).$$

At order ε^3 the mean-field model writes $(\partial_{t_0} - f_u)u^{(3)} = g^{(3)}$ with

$$g^{(3)} = \begin{pmatrix} -\partial_{t_2}x_0^{(1)} - 2\gamma A_1^{(2)}x_1^{(1)} - 2\gamma x_1^{(1)}x_1^{(2)} - \frac{1}{2}\Delta_T y_0^{(2)} \\ -\partial_{t_2}x_1^{(1)} + A_0^{(2)}x_1^{(1)} + A_1^{(2)}x_0^{(1)} + x_0^{(2)}x_1^{(1)} + x_1^{(2)}x_0^{(1)} - RF_x^{(3)} - \Delta_T y_1^{(2)} \\ g_{y0}^{(3)} \\ g_{y1}^{(3)} \end{pmatrix}, \tag{A6}$$

where $F_x^{(3)} = t_f(2A_1^{(2)}x_1^{(1)} + 2x_1^{(1)}x_1^{(2)}) + t_3 x_1^{(1)3}$, with $t_3 = 8\overline{A}_1^2 S^2/D^4 - S/D^2$.

The solvability condition becomes

$$\partial_{t_2}A = \mu A - c_3|A|^2 A - c_1\Delta_T^{(1)2}A, \tag{A7}$$

with

$$\mu = \frac{1}{p_0 q_0 + p_1 q_1}\{q_0(-2\gamma A_1^{(2)}p_1) + q_1(A_0^{(2)}p_1 + A_1^{(2)}p_0 - 2Rt_f A_1^{(2)}p_1)\},$$

$$c_3 = \frac{-1}{p_0 q_0 + p_1 q_1}\{-2\gamma q_0(x_1^{(2,2\omega)}p_1^* + x_1^{(2,0)}p_1) + q_1\sigma\},$$

$$c_1 = \frac{-1}{p_0 q_0 + p_1 q_1}(\frac{1}{2}q_0 y_0^{(2,\omega)} + q_1 y_1^{(2,\omega)}), \tag{A8}$$

where

$$\sigma = [x_0^{(2,2\omega)}p_1^* + x_1^{(2,0)}p_1 + x_1^{(2,2\omega)}p_0^* + x_1^{(2,0)}p_0 - 2Rt_f(x_1^{(2,2\omega)}p_1^* + p_1 x_1^{(2,0)}) - 3Rt_3 p_1^2 p_1^*].$$

In terms of the original variables, one obtains the amplitude equation

$$\partial_t A = \varepsilon^2 \mu A - c_3|A|^2 A - c_1\Delta_T^2 A. \tag{A9}$$

APPENDIX B: STABILITY OF WAVE SOLUTIONS OF Eq. (9)

Equation (9) admits a family of plane-wave solutions, like the CGL Eq. (11),

$$A = Fe^{i(\mathbf{Q}\cdot r - \omega t + \phi)}, \tag{B1}$$

where the amplitude F and the frequency ω depend on the wave number $Q = |\mathbf{Q}| < 1$,

$$F^2 = 1 - Q^4,$$

$$\omega = c + (b - c)Q^4. \tag{B2}$$

The stability criterion of these solutions is derived from a standard stability analysis involving the value of the underlying wave vector $\mathbf{Q}$ and, of course, parameters b and c, as in the case of the usual CGL equation. The perturbed solution $A = Fe^{i(\mathbf{Q}\cdot r - \omega t)} + \delta a_+ e^{i(\mathbf{Q}+k)\cdot r + (\lambda + i\omega)t} + \delta a_- e^{i(\mathbf{Q}-k)\cdot r + (\lambda^* - i\omega)t}$ leads to the eigenvalue problem

$$\begin{vmatrix} \lambda + \alpha & F^2(1 + ic) \\ F^2(1 - ic) & \lambda + \beta \end{vmatrix} = 0, \tag{B3}$$

with

$$\alpha = F^2 + f_+ + i(cF^2 + bf_+),$$

$$\beta = F^2 + f_- - i(cF^2 + bf_-), \tag{B4}$$

and $f_\pm = k^2 \pm 2\mathbf{Q}\cdot\mathbf{k}, k = |\mathbf{k}|$. The solution of Eq. (B3). is

$$\lambda(\mathbf{k}) = -b' \pm \sqrt{b'^2 - g}, \tag{B5}$$

with $b' = F^2 + k^2 + 2ib\mathbf{Q}\cdot\mathbf{k}, g = \alpha\beta - F^4(1 - c^2)$. Expanding the complex growth rate for small k gives

$$\lambda = -iV_g k - D_2 k^2 - i\Omega_g k^3 - D_4 k^4 + O(k^5), \tag{B6}$$

with

$$V_g = 4(b - c)Q^2\mathbf{Q}_k,$$

$$D_2 = 2(1 + bc)(Q^2 + 2\mathbf{Q}_k^2) + 8\mathbf{Q}_k^2 Q^4(1 + c^2)/(1 - Q^4),$$

$$\Omega_g = 4\mathbf{Q}_k\left\{(b - c) + \frac{2(1 + c^2)Q^2}{1 - Q^4}[4cQ^4\mathbf{Q}_k^2/(1 - Q^4) - b(Q^2 + 2\mathbf{Q}_k^2)]\right\},$$

$$D_4 = 1 + bc + \frac{2}{1-Q^4}(1+c^2) - 8Q^2\mathbf{Q}_k^2 + b^2(Q^2 + 2\mathbf{Q}_k^2)^2$$

$$- \frac{48}{(1-Q^4)^2}bcQ^4\mathbf{Q}_k^2(Q^2+2\mathbf{Q}_k^2)$$

$$+ \frac{32}{(1-Q^4)^3}(1+6c^2+5c^4)Q^8\mathbf{Q}_k^4, \tag{B7}$$

where $\mathbf{Q}_k = \mathbf{Q}\cdot\mathbf{k}$ is the component of $\mathbf{Q}$ parallel to $\mathbf{k}$. The longitudinal perturbations with $\mathbf{k}//Q$ are the most dangerous ones. The solutions (B1) are long-wave stable as long as the phase diffusion coefficients $D_{2//}, D_{4//}$ are positive. Equations (B7) give

$$D_{2//} = 2Q^2[3(1+bc) - 4Q^4(1+c^2)/(1-Q^4)],$$

$$D_{4//} = 1 + bc + 2(1+c^2)(9b^2 - 8)\frac{Q^4}{1-Q^4} - 144bc(1+c^2)$$

$$\times \frac{Q^8}{(1-Q^4)^2} + 32(1+6c^2+5c^4)\frac{Q^{12}}{(1-Q^4)^3}. \tag{B8}$$

The stability of the homogeneous oscillating state ($Q=0$) results from the fourth-order term (while it is given by $D_{2//}$ in the case of the CGL equation) which leads to the condition $1+bc>0$. At second order the range of stable wave numbers obeys the relation $Q<Q_E$ with

$$Q_E^4 = \frac{1+bc}{\frac{7}{3}+bc+\frac{4}{3}c^2}. \tag{B9}$$

[1] See, for example, M. I. Rabinovich, A. B. Ezersky, and P. D. Weidman, *The Dynamics of Patterns* (World Scientific, London, 2000), and references herein.

[2] For an overview of experimental and theoretical results on propagation of vortices in nonlinear media, see the review paper by Yu. S. Kivshar and B. Luther-Davies, Phys. Rep. **298**, 81 (1998).

[3] P. Coullet, L. Gil, and F. Rocca, Opt. Commun. **73**, 403 (1989).

[4] H. Chaté and P. Manneville, Physica A **224**, 348 (1996).

[5] I. S. Aranson and L. Kramer, Rev. Mod. Phys. **74**, 99 (2002).

[6] K. Staliunas, Phys. Rev. A **48**, 1573 (1993); J. Lega, J. V. Moloney, and A. C. Newell Phys. Rev. Lett. **73**, 2978 (1994).

[7] K. Staliunas, M. F.H. Tarroja, G. Slekys, C. O. Weiss, and L. Dambly Phys. Rev. A **51**, 4140 (1995); C. O. Weiss, M. Vaupel, K. Staliunas, G. Slekys, and V. B. Taranenko Appl. Phys. B: Lasers Opt. **68**, 151 (1999).

[8] M. Tlidi, M. Giorgiou, and P. Mandel, Phys. Rev. A **48**, 4605 (1993).

[9] S. Longhi, Phys. Rev. A **53**, 4488 (1996); Z. H. Musslimani, Physica A **249**, 141 (1998); V. J. Sanchez-Morcillo, E. Roldan, G. J. de Valcarcel, and K. Staliunas, Phys. Rev. A **56**, 3237 (1997).

[10] M. Brambilla, F. Battipede, L. A. Lugiato, V. Penna, F. Prati, C. Tamm, and C. O. Weiss, Phys. Rev. A **43**, 5090 (1991).

[11] F. T. Arecchi, G. Giacomelli, P. L. Ramazza, and S. Residori, Phys. Rev. Lett. **67**, 3749 (1991).

[12] D. Lu, W. Lu, and R. Harrison, Phys. Rev. Lett. **77**, 5051 (1996); D. Yu, W. Lu, and R. G. Harrison J. Opt. B: Quantum Semiclassical Opt. **1**, 25 (1999).

[13] P. Lodahl, M. Bache, and M. Saffman, Phys. Rev. Lett. **85**, 4506 (2000).

[14] F. Huneus, B. Schapers, T. Ackemann, and W. Lange, Appl. Phys. B: Lasers Opt. **76**, 191 (2003).

[15] Q. Ouyang, H. L. Swinney, and G. Li, Phys. Rev. Lett. **84**, 1047 (2000).

[16] G. Izus, M. San Miguel, and M. Santagiustina, Opt. Lett. **25**, 1454 (2000)

[17] S. Longhi, Phys. Rev. E **63**, 055202 (2001).

[18] P. Coullet and K. Emilsson, Physica D **61**, 119 (1992).

[19] M. Tlidi, P. Mandel, and M. Haelterman, Phys. Rev. E **56**, 6524 (1997); M. Tlidi and P. Mandel, Phys. Rev. A **59**, R2575 (1999).

[20] A. Barsella, C. Lepers, M. Taki, and M. Tlidi, Opt. Commun. **232**, 381 (2004).

[21] M. Tlidi, M. Taki, M. Le Berre, E. Ressayre, A. Tallet, and L. Di Menza, J. Opt. B: Quantum Semiclassical Opt. **6**, 5421 (2004).

[22] Mustapha Tlidi and Majid Taki, Phys. Rev. Lett. **91**, 023901 (2003).

[23] M. Tlidi, M. Le Berre, E. Ressayre, A. Tallet, and L. Di Menza, Phys. Rev. A **61**, 043806 (2000).

[24] An isolated peak, or localized structure, is a homoclinic solution connecting the two HSS's, formed when using a local perturbation with large amplitude. In one transverse dimension the profile of the signal field reported in Ref. [19] shows positive wing value equal to $\overline{A}_1$ and negative peak value equal to $-A_1$. In two dimensions, the modulus of the peak is enlarged due to curvature effects. Such solutions also exist in the case of stable HSS's, as reported in the DOPO case [25] without a saturable absorber. On the other hand , in presence of a Turing instability of the HSS's, the DOPOSA displays periodic patterns which are generated subcritically with respect to E_T. Hexagons, rolls, or squares are observed when starting from similar periodic initial conditions with large amplitude. We have observed that the periodic solution is not formed around one of the HSS's, but is symmetric with respect to the trivial solution. Consequently the periodic pattern results from a locking between the two sets of Turing modes associated with the two HSS's.

[25] K. Staliunas and V. J. Sanchez-Morcillo, Phys. Rev. A **57** 1454 (1998); M. Le Berre, D. Leduc, E. Ressayre, and A. Tallet, J. Opt. B: Quantum Semiclassical Opt. **1** 153 (1999); G. L. Oppo, A. J. Scroggie, and W. J. Firth, *ibid.* **1** 133 (1999).

[26] C. Brito, I. S. Aranson, and H. Chate, Phys. Rev. Lett. **90**, 068301 (2003).

[27] A. L. Belmonte, Q. Ouyang, and J. M. Flesselles J. Phys. II **7**, 1425 (1997).

[28] A. Karma, Phys. Rev. Lett. **71**, 1103 (1993).

[29] Y. A. Astrov, I. Muller, E. Ammelt, and H. G. Purwins, Phys. Rev. Lett. **80**, 5341 (1998).

[30] L. Gil, K. Emilsson, and G. L. Oppo, Phys. Rev. A **45**, R567 (1992); I. Aranson, D. Hochheiser, and J. V. Moloney, *ibid.* **55**, 3173 (1997); V. M. Eguiluz, E. Hernandez-Garcia, and O. Piro, Int. J. Bifurcation Chaos Appl. Sci. Eng. **9**, 2209 (1999); M. Hendrey, K. Nam, P. Guzdar, and E. Ott, Phys. Rev. E **62**, 7627 (2000).

[31] A. Hagberg and E. Meiron, Physica A **249**, 118 (1998); Phys. Rev. E **57** 299 (1998).